Porous Materials

DOI: 10.1002/anie.201408713

Porous and Shape-Anisotropic Single Crystals of the Semiconductor Perovskite $CH_3NH_3PbI_3$ from a Single-Source Precursor**

*Tom Kollek, Dominik Gruber, Julia Gehring, Eugen Zimmermann, Lukas Schmidt-Mende, and Sebastian Polarz**

Abstract: *Significant progress in solar-cell research is currently made by the development of metal–organic perovskites (MOPs) owing to their superior properties, such as high absorption coefficients and effective transport of photogenerated charges. As for other semiconductors, it is expected that the properties of MOPs may be significantly improved by a defined nanostructure. However, their chemical sensitivity (e.g., towards hydrolysis) prohibits the application of methods already known for the synthesis of other nanomaterials. A new and general method for the synthesis of various $(CH_3NH_3)PbI_3$ nanostructures from a novel single-source precursor is presented. Nanoporous MOP single crystals are obtained by a crystal-to-crystal transformation that is accompanied by spinodal demixing of the triethylene glycol containing precursor structure. Selective binding of a capping agent can be used to tune the particle shape of the MOP nanocrystals.*

A new class of perovskites comprising organic and inorganic constituents was introduced by Mitzi and co-workers in 1999,[1] with $(CH_3NH_3)PbI_3$ (MAPI) as a representative example. It took several years until the enormous potential of metal–organic perovskites (MOPs) for novel applications, mainly for solar cells, was revealed.[2] The superior performance of MOPs such as MAPI results from a unique combination of optical and semiconducting properties. The high absorption coefficient and ambivalent character, which enables the conduction of both electrons and holes, opened a new field of solid-state absorbers, which are used in high-performance solar cells with efficiencies of more than 16%.[2b,c] Owing to further increases in efficiency, MOPs are also explored in numerous fields beyond photovoltaics and optoelectronics.[3]

Nanostructuration is of enormous importance for almost any semiconductor.[4] One of the most intriguing examples was published recently by Snaith et al. for a different, highly functional semiconductor.[5] The authors described porous titania single crystals and their remarkable properties for optoelectronic applications. Consequently, structuration on the nano- and mesoscale is also highly desirable for MOPs.[2c] Attempts were made to form thin films or mesostructured devices using nanoparticles as a template.[2a–c] Unfortunately, crystallization by solution–precipitation methods is often difficult to be controlled as it leads to large morphological variations.[2b] Furthermore, MOPs are relatively labile compounds in comparison to stable oxides such as TiO_2. This requires cautious handling and renders the synthesis of defined nanostructures more difficult. The CH_3NH_3I constituent rapidly photodecomposes into CH_3NH_2 and HI, leaving behind PbI_2, when traces of water are present.[6] More importantly, the high solubility of MAPI in polar solvents poses major difficulties regarding the direct transfer of established nanostructuration methods.[7]

Successful methods for the synthesis of refined $(CH_3NH_3)PbI_3$ nanostructures are missing, and a material similar to the described TiO_2 porous single crystal or to microporous crystals such as metal–organic frameworks (MOFs) is currently out of reach.[8] As a facile new concept towards MAPI nanostructures we present a special compound with single-source precursor properties (Figure 1).

The novel precursor is key for controlling particle nucleation and further growth up to the micrometer scale. The structure of the precursor phase was clarified by single-crystal X-ray diffraction analysis (Figure 1). The crystal structure of the new organolead perovskite has an orthorhombic unit cell with a relative composition of $(CH_3NH_3)PbI_3(TEG)_2$ (**1**; TEG = triethylene glycol). Pb^{2+} is coordinated by six iodide ions in octahedral geometry ($[PbI_6]$ octahedron); these octahedra form one-dimensional chains by face sharing. Two TEG molecules coordinate to one counterion $(CH_3NH_3)^+$ in a cryptand-like fashion. The crystal structure of **1** is almost comparable to a solid solution of $[PbI_3]^-_n$ chains in TEG as the solvent (see Figure 1a). This special structural feature is also responsible for a fairly low temperature for the solid→liquid phase transition, which was determined by differential scanning calorimetry (DSC) to occur at 70°C (see the Supporting Information, Figure S1). The melting process could be followed by polarization microscopy (POLMIC). **1** forms needle-shaped crystals with optical anisotropy (space group *Pbca*) and birefringence. The melting of **1** into an isotropic liquid can be followed by the disappearance of the birefringence (see Figure S2). The ability to transform **1** into a liquid phase is an important feature for future nanostructuration approaches, for example, for infiltration in template structures. The optical properties of **1** were investigated by diffuse-reflectance UV/Vis spectroscopy (Figure S1). According to a Kubelka–Munk data

[*] T. Kollek, D. Gruber, J. Gehring, E. Zimmermann, Prof. Dr. L. Schmidt-Mende, Prof. Dr. S. Polarz
University of Konstanz
Universitätsstrasse 10, 78457 Konstanz (Germany)
E-mail: sebastian.polarz@uni-konstanz.de
Homepage: http://cms.uni-konstanz.de/polarz/

[**] We thank the Baden-Württemberg foundation for financial support (projects "BioMat-S7" and "SUPERSOL"; program "Biomimetic Materials Synthesis"). Dr. I. Göttker is acknowledged for single-crystal X-ray analysis.

Supporting information for this article is available on the WWW under http://dx.doi.org/10.1002/anie.201408713.

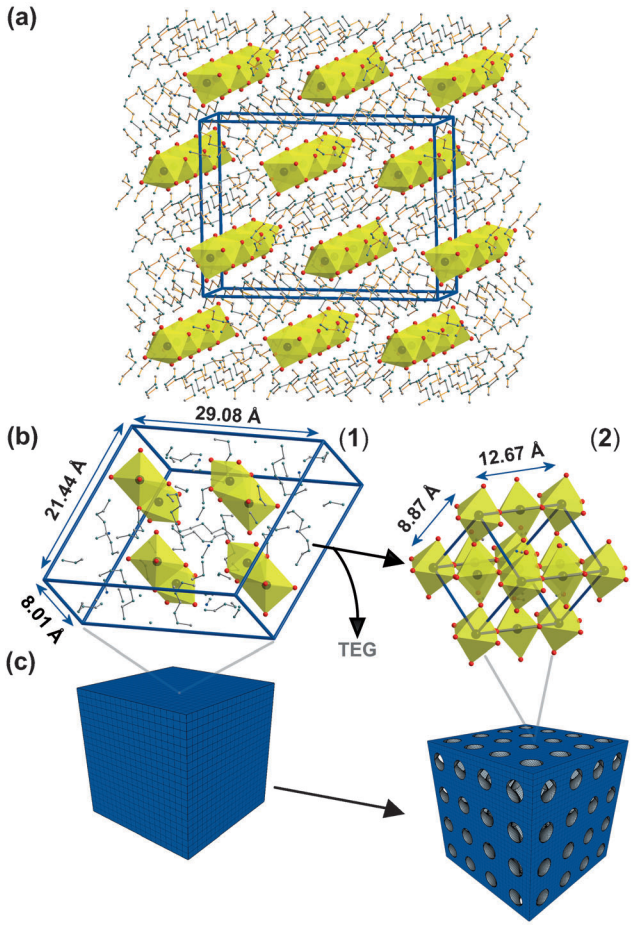

Figure 1. a) The novel perovskite precursor phase $(TEG)_2(CH_3NH_3)PbI_3$ (**1**). Pb black, I red, N blue, carbon dark grey, oxygen light grey; $[PbI_6]$ octahedra: yellow faces; unit cell: blue lines. b) Crystal-to-crystal transition into the perovskite product $(CH_3NH_3)PbI_3$ (**2**) accompanied by the loss of TEG. c) Formation of porous perovskite single crystals.

evaluation,[9] **1** is a direct semiconductor with a band gap of $E_{gap} = 2.55$ eV.

The transformation of $(TEG)_2(CH_3NH_3)PbI_3$ into $(CH_3NH_3)PbI_3$ can be triggered by the differential solubility of the two components: Using a suitable anti-solvent, such as dichloromethane (CH_2Cl_2) or ethyl acetate (AcOEt), the injection of $(TEG)_2(CH_3NH_3)PbI_3$ initiates the crystallization process. As TEG readily dissolves in CH_2Cl_2, whereas $(CH_3NH_3)PbI_3$ (**2**) does not, TEG is removed with time. The removal of TEG leads to a crystal–to crystal transition (**1**→**2**) into the final perovskite $(CH_3NH_3)PbI_3$, which is characterized by the three-dimensional linkage of $[PbI_6]$ octahedra (see Figure 1b). A kinetic study by time-dependent UV/Vis spectroscopy (Figure S3a) revealed that **2** is directly formed from **1** without any detectable intermediates.

Furthermore, high-resolution transmission electron microscopy (HR-TEM) images acquired at different times indicate that crystallites of **1** are formed first, which are then directly converted into the product (**2**). The HR-TEM observations are in good agreement with findings from powder X-ray diffraction analysis (PXRD; see Figure 2). Initially, only signals corresponding to precursor structure

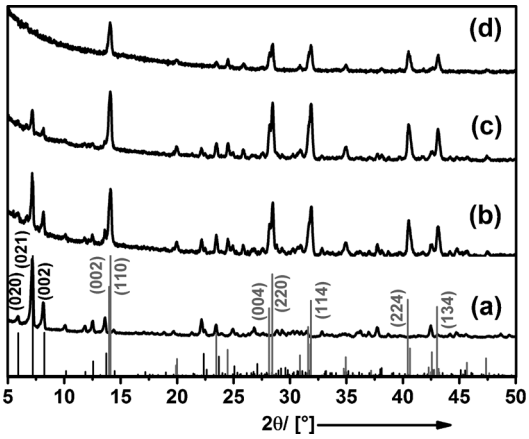

Figure 2. PXRD patterns for the precursor phase **1** (black bars) and of the product phase **2** (grey bars). The reference pattern for **1** was calculated from single-crystal X-ray data. The reference pattern of **2** was obtained from data of a material prepared by the known routes for $(CH_3NH_3)PbI_3$.[3] a–d) Experimental PXRD patterns of the precursor phase **1** directly after addition of the anti-solvent (b) and after washing with solvent once (c) or twice (d).

1 are observed. After repeated exposure to CH_2Cl_2 and gradual dissolution of TEG, these signals disappear, and the diffraction pattern of **2** appears. Our assumption of a direct crystal-to-crystal transition is corroborated by an experiment performed on macroscopic single crystals of **1** (Figure S3c). Using conventional optical-light microscopy, it was observed that the yellow crystals of **1** are converted into black crystals (**2**) while the shape of the crystals is preserved.

Precipitation from the $(TEG)_2(CH_3NH_3)PbI_3$ solution results in a powder (designated as MAPI-0) consisting of nanoparticles that are ill-defined with respect to size and shape (Figure S4). Control over the particle growth is essential for synthesizing tailor-made MAPI nanostructures. For semiconductor quantum dots (e.g., CdSe),[10] it is well known that the growth of particles can be regulated using suitable capping agents. A capping agent is typically of amphiphilic character and consists of a long-chain alkyl tail to guarantee colloidal stability (e.g., $-CH_2(CH_2)_nCH_3$) and a functional head group, which is capable of interacting with dangling bonds at the surface of the material. A logic criterion for a capping agent is that the interacting groups are closely related to the units occurring in the crystal lattice. Thus, in the case of $(CH_3NH_3)PbI_3$, a promising capping agent should contain ammonium ions (for interactions with anionic $[PbI_6]$ octahedra) and I^- species (for interactions with surface $CH_3NH_3^+$ or Pb^{2+}). Furthermore, the capping agent has to be soluble in the anti-solvent. All of these requirements are fulfilled by dodecylammonium iodide (DAI). DAI was thus used as the capping agent, and its concentration was varied systematically (see the Experimental Section), revealing a pronounced effect on the resulting $(CH_3NH_3)PbI_3$ morphologies. At low DAI concentrations (sample MAPI-1), the particles have a defined shape in the size range of 50–400 nm (Figure 3; see also Figure S5a). The cubic morphology with sharp edges and flat surfaces gives a first indication that the particles are crystalline. Electron diffraction (ED) measure-

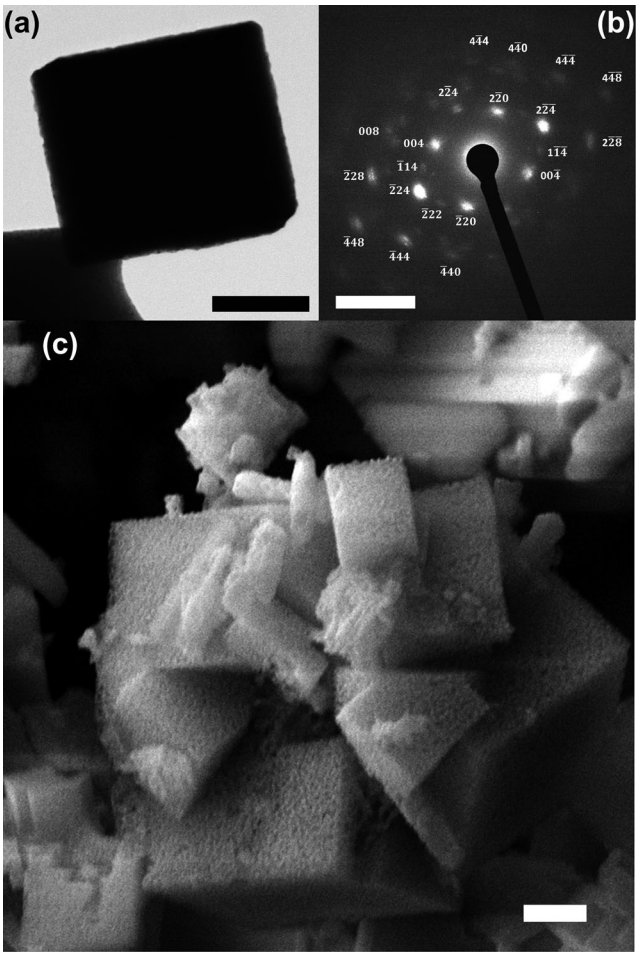

Figure 3. a) TEM micrograph of a MAPI-1 cube (scale bar: 200 nm). b) Corresponding ED pattern (scale bar: 5 nm^{-1}) with assigned reflections. c) SEM micrograph of an ensemble of porous perovskite single crystals (scale bar: 400 nm).

ments with a single particle indeed reveals a pattern with diffraction spots characteristic for $(CH_3NH_3)PbI_3$ in the form of one single crystal (Figure 3a,b). The high crystallinity and single-phase purity were confirmed by PXRD measurements (Figure S5b), where only narrow signals exclusively corresponding to **2** were detected.

Initial SEM investigations showed that the surfaces of the particles are flat, but also rough. Further SEM images were then recorded at higher magnifications (Figure 3c), which clearly reveal that each particle is porous with pore sizes of 20–30 nm. It was also confirmed by SEM on sliced particles obtained by using a focused ion beam (FIB) that the observed cavities are not only present at the surfaces. Although some degree of radiation damage cannot be excluded, the pores were also found to be present in the bulk of the cubic particles (Figure S5c). Unfortunately, characterization techniques commonly used for porous materials, such as gas sorption analysis, failed or only afforded irreproducible results as the porous structure is highly sensitive to the drying conditions (e.g. solvent, temperature, time). In particular, traces of water lead to very fast restructuring and the collapse of the porous network. Such processes are not uncommon for materials characterized by relatively weak cohesion forces, for example, for many coordination polymers or organic polymers. Open porosity can hardly be maintained owing to the high surface energy associated with nanometer-sized pores.[11] However, to investigate the porosity of the material with an independent method, we investigated the desorption of a liquid (toluene; b.p. 110.6 °C) confined inside the pores of MAPI-1 using thermogravimetric analysis (TGA) under argon atmosphere. The results are shown in Figure S5d. A non-porous material (MAPI-2) was used as a reference revealing an expected mass loss at $T = 337$ °C:[12] $CH_3NH_3PbI_3 \rightarrow PbI_2 + CH_3NH_2(\uparrow) + HI(\uparrow)$. Although the composition of MAPI-1 is the same as that of the reference compound (see Figure S8), the TGA data significantly differ. Two important features can be observed: 1) A new mass loss occurs in the temperature range starting at 110 °C with a maximum mass loss rate at $T =$ 159 °C. This step can be assigned to the release of toluene adsorbed in the pores, and the increase in evaporation temperature is due to the capillary forces that are described by the Kelvin equation (Figure S5d). 2) The temperature for MAI decomposition is much lower (269 °C). This observation can also be interpreted as an indication for the porosity present in the material. It is well known that the temperature of TGA mass losses is strongly influenced by equilibrium factors (Le Chatelier's principle). For example, porous structures promote the formation of gaseous products, which results in shifts of the equilibria and the associated mass losses (to lower temperatures).

As the pores feature no periodic order, and their size distribution is polydisperse, it is worth mentioning that the transformation of **1** into **2** (see also Figure 1b) results in a significant shrinkage of the unit-cell volume by 80 % ($V_u(\mathbf{1}) = 5123$ Å$^3 \rightarrow V_u(\mathbf{2}) = 997$ Å^3). This transformation is accompanied by the release of a substantial number of TEG molecules. As the transformation also implies a change in the crystal system (orthorhombic→tetragonal), it is not topotactic by definition. However, it might be compared to phenomena observed when a melt solidifies near a eutectic composition. In such processes, it may be observed that macroscopic phase separation can be avoided, and segregation takes place at the micro- or nanoscale instead. This so-called spinodal decomposition seems to be responsible for the generation of cavities in MAPI-1. In agreement with this interpretation, the precursor phase **1** resembles a very special (solid and crystalline) "melt" of $(CH_3NH_3)PbI_3$ in TEG, which can be compared to certain nanoporous silica materials presented by Nakanishi and co-workers.[13] Pores were formed by the spinodal microphase separation of silica, which had been obtained by a sol–gel reaction of a precursor, and certain polymers or oligomers as the demixing components, commonly ethylene glycol derivatives.[14] There are some obvious similarities to the system described here. Additional evidence for the proposed mechanism was acquired by TEM. During the formation of $(CH_3NH_3)PbI_3$ (**2**) from the precursor phase **1**, the crystalline particles (Figure S3b) with an angular shape can form slit-like pores (Figure S5e). This very unusual particle morphology, which is associated with a high surface energy, can be rationalized as the beginning of the spinodal decomposition.

Next, the concentration of DAI was gradually increased (MAPI-2, MAPI-3, MAPI-4). The particles in MAPI-2 still possess a cubic morphology (Figure 4a; see also Figure S6). The size distribution of the obtained perovskite crystals is much narrower, and the majority of the particles are smaller than those in MAPI-1 (200 nm). As a consequence of the reduced size, the TEG molecules can much more easily leave the particles when the transformation **1**→**2** occurs. This suppresses spinodal decomposition and thereby the generation of the porous substructure. SEM micrographs taken at larger magnifications show that the particles are compact (see Figure S6). Similar to particle-based aerogel-like materials, the perovskite nanocrystals form networks with residual porosity (Figure 4a).[15] When even higher concentrations of DAI are used in the synthesis (Figure 4b,c) the cubic symmetry of the particle shape is broken, and the perovskite forms crystals with increasing aspect ratios. MAPI-3 consists of crystals with a rectangular prismatic shape (Figure 4b), and MAPI-4 is formed as sheets (Figure 4c). The main direction of crystal growth could be identified by the analysis of the PXRD signals corresponding to the (*hk*0) lattice planes in comparison to the perpendicular lattice planes (002). Therefore, diffraction signal pairs for (002), (110) or (004), (220) are suitable. On gradually increasing the DAI concentration, the relative intensities of the diffraction signals with a pure *c*-component (e.g., (004)) decrease (Figure S7). For quantitative evaluation, for example, for a calculation of the aspect ratio, deconvolution becomes necessary because of the vicinity of the signals. The preferential growth of the particles could thus be determined to occur in the crystallographic *a,b*-direction.

To rationalize the effect of DAI, the slightly tetragonal distorted crystal structure of $(CH_3NH_3)PbI_3$ at room temperature has to be considered (Figure 1b). The distances between adjacent $[PbI_6]$ octahedra that belong to different lattice planes on the particle surface are not the same. The distance between the $[PbI_6]$ octahedra (which also corresponds to the distance between dangling I^- at the surface; see Scheme 1 in Figure S7) is 0.62 nm for the (004) lattice plane and consequently differs from that of the (100) plane (0.89 nm, 0.73 nm), for example. The position of the I^- ions on the $(CH_3NH_3)PbI_3$ surface is important because the cationic head group of DAI will coordinate at this position.

The distances can now be compared to a reference system described in the literature:[16] The area per alkyl surfactant in monolayers on an inorganic surface such as mica can be considered. The surfactant–surfactant distance is 0.67 nm. Assuming that the ideal DAI–DAI distance is similar for surface-adsorbed DAI, better packing is expected on the (004) surface. In turn, this will lead to an effective passivation of (004) while on the perpendicular surfaces, the packing of DAI is assumed to be less dense. This leads to further apposition of $(CH_3NH_3)PbI_3$ units and preferential growth in the *a*- and *b*-directions as a consequence. The anisotropic crystal growth can also affect the distortion of the tetragonal crystal structure, which be taken into account by calculating the pseudo-cubic lattice parameters (*c**/*a**) from the PXRD data. The distortion is strongly affected by the temperature and reported to be approximately 0.6% under ambient conditions.[3] We observed an increase in distortion from 0.93% (MAPI-2) to 1.82% (MAPI-4) with an increase in DAI concentration.

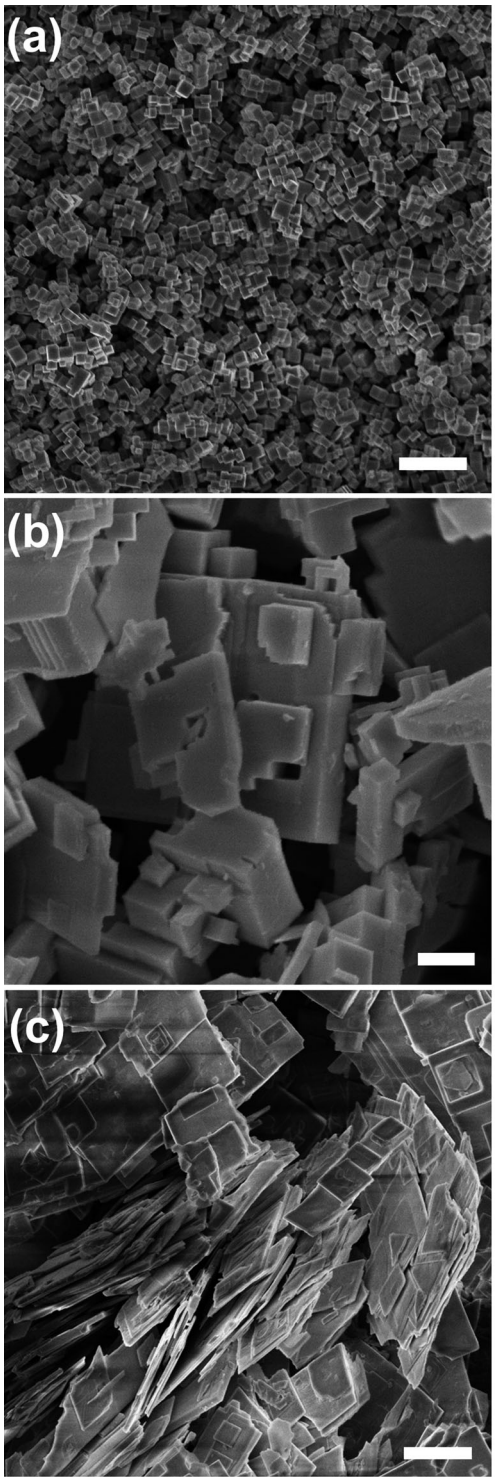

Figure 4. SEM micrographs of a) MAPI-2 (scale bar: 2 μm), b) MAPI-3 (scale bar: 400 nm), and c) MAPI-4 (scale bar: 4 μm).

As the amount of DAI used in the synthesis is higher than that needed for stabilizing the interfaces of $(CH_3NH_3)PbI_3$, its function as a capping agent was questioned. Using FT-IR and ^1H NMR spectroscopy (Figure S8), it could be shown that the

relative amount of DAI compared to methyl ammonium iodide (MAI) increases from MAPI-1 to MAPI-3, but remains small (<0.01) in all cases. The results for MAPI-4 revealed a DAI/MAI ratio of 1.53; this amount is so large that it cannot be explained by the use of DAI only for surface stabilization. Billing et al. described a compound that consists of a monolayer of 2D-linked [PbI_6] octahedra with DAI bound on each side of the layer interacting with each other by van der Waals forces ($(DAI)_2PbI_4$).[17] Whereas the PXRD patterns of MAPI-1, MAPI-2, and MAPI-3 contain exclusively the signals associated with $(CH_3NH_3)PbI_3$, the pattern of MAPI-4 shows a similarity to the reported crystal structure of $(DAI)_2PbI_4$. In particular, one characteristic signal was observed at low angles, which was also confirmed by small-angle X-ray scattering (SAXS). This reflection allows the determination of the thickness of separated layers in the *z*-direction, which comprise linked [PbI_6] octahedra and $CH_3NH_3^+$ (Figure S8c). According to SAXS and PXRD analysis , MAPI-4 consists of a double layer of corner-sharing [PbI_6] octahedra that extend in the *a,b*-direction and are blocked by a dense layer of DAI in the *c*-direction. The latter results were corroborated by elemental analysis. As the N/C ratio systematically decreases with an increase in the DAI content the number of [PbI_6] layers between the DAI layers for the different presented $(CH_3NH_3)PbI_3$ materials can be concluded. For MAPI-1, MAPI-2, and MAPI-3, the count is in the order of 230–80 layers, which is in good agreement with the assumption that DAI acts only as a capping agent in these systems. For MAPI-4, it could be confirmed that a double layer was present. Thus, similar to the structure reported by Billing et al.,[17] DAI has become an integral part of the structure.

Finally, first studies were performed to evaluate the potential of the presented MAPIs as functional materials in photophysical applications. Preliminary characterizations and tests for their application in hybrid solar cells were conducted with thin-film architectures. It should be considered that optimization and long-term experience regarding device fabrication are necessary for obtaining reliable results and high performances in the future. Furthermore, the MAPI materials still contain DAI as the capping agent. Owing to the insulating character of the alkyl chain, it is expected that the efficiency of the devices might be reduced significantly. Hence, we see the following results only as a proof of principle, and further investigations are part of our ongoing research. UV/Vis/NIR spectra were acquired for all MAPI samples (Figure S9). In agreement with the properties of $(CH_3NH_3)PbI_3$ reported in the literature, all MAPI materials herein presented are direct semiconductors with a band gap of 1.52 eV. However, for MAPI-4, a shift of the band edge to higher energies, which is due to the reduced dimension of the 3D perovskite phase and the associated quantum size effect, is detected. For assembling hybrid solar cells, indium tin oxide (ITO) was used as a transparent electrode and coated with TiO_2 as the blocking layer. Spin-coating of MAPI-2 particles followed. The preliminary device was completed by covering the MAPI-2 layer with SpiroOMeTAD as a hole conductor[18] and an Ag/Au back-contact (Figure S10). Spectrally resolved measurements of the external quantum efficiency (EQE) were conducted to confirm that the MAPI-2 layer (crystalline cubes) works as a light-harvesting material and delivers a stable photocurrent over the whole visible range. Despite the lack of any optimization, a working photovoltaic device could be constructed. As expected, the performance indicators ($I_{sc}=2.90\ mA\,cm^{-2}$, $V_{oc}=0.77\ V$, $FF=30\,\%$, efficiency $=0.68\,\%$) are significantly lower than the values reported for state-of-the-art thin-film perovskite solar cells.[2c]

The main focus of the current manuscript was the preparation of crystalline metal–organic perovskite particles with a special shape and nanostructure. A new and crystalline triethylene glycol containing $(CH_3NH_3)PbI_3$ phase could be presented as a versatile and liquefiable single-source precursor. It was shown that the use of a suitable capping agent enables the control of the shape and the aspect ratio of the perovskite nanocrystals. The latter is a particularly appealing aspect because it was recently recognized that particle shape can be an important tool to control functional properties.[19] Furthermore, our results on MAPI open-framework nanostructures contradict the hypothesis that single-crystalline states are distinct or even incompatible with nanostructured states.

Experimental Section

Synthesis of TEG precursor solutions: For the synthesis of the TEG precursor solution, 12 mL triethylene glycol (TEG, Merck, $\geq 99\,\%$) and 1.2 mmol lead(II) iodide (PbI_2, Aldrich, 99 %) were degassed under stirring for three hours at 60 °C. After cooling down to room temperature, methyl ammonium iodide (MAI, 1.6 mmol)[2d] was dissolved yielding a yellow, clear solution.

Dodecylammonium iodide (DAI) was synthesized according to a procedure modified from that described by Aoyagi and co-workers.[20] In a typical synthesis, dodecylamine (29.6 mmol, 5.49 g) was dissolved in 1,4-dioxane (150 mL), and HI (57 wt %, 7.4 mL, 54 mmol) was added dropwise to the solution under vigorous stirring at room temperature. After stirring overnight, the solvent was removed with a rotary evaporator at 60 °C. The obtained raw product was washed with Et_2O, recrystallized in EtOH/Et_2O, and dried at 40 °C under vacuum yielding a white powder (7.23 g, 23 mmol).

MAPI synthesis: The appropriate amount of DAI was dissolved in TEG precursor solution (180 μL). This solution was rapidly injected into CH_2Cl_2 (30 mL) containing DAI (9 μmol). The resulting concentration of DAI depends on the targeted sample: 0 $mmol\,L^{-1}$ (MAPI-0), 0.5 $mmol\,L^{-1}$ (MAPI-1), 2.0 $mmol\,L^{-1}$ (MAPI-2), 3.8 $mmol\,L^{-1}$ (MAPI-3), 9.8 $mmol\,L^{-1}$ (MAPI-4). The solution turned from yellow to black, indicating the transformation of the TEG precursor into the product. After 12 h of stirring, the black precipitate was centrifuged for 5 min at 6000 rom, washed three times with CH_2Cl_2, and dried under vacuum. All samples were stored under argon atmosphere to prevent decomposition because of moisture. Detailed information on the synthesis of the various MAPI samples can be found in the Supporting Information (S11).

For information on the single-crystal X-ray diffraction experiments, see the Supporting Information (S12).[21]

Received: September 1, 2014
Published online: December 3, 2014

Keywords: anisotropic nanoparticles · metal–organic perovskites · porous single crystals · semiconductor nanostructures

[1] C. R. Kagan, D. B. Mitzi, C. D. Dimitrakopoulos, *Science* **1999**, *286*, 945.
[2] a) M. M. Lee, J. Teuscher, T. Miyasaka, T. N. Murakami, H. J. Snaith, *Science* **2012**, *338*, 643; b) J. Burschka, N. Pellet, S. J. Moon, R. Humphry-Baker, P. Gao, M. K. Nazeeruddin, M. Graetzel, *Nature* **2013**, *499*, 316; c) M. Z. Liu, M. B. Johnston, H. J. Snaith, *Nature* **2013**, *501*, 395; d) S. D. Stranks, G. E. Eperon, G. Grancini, C. Menelaou, M. J. P. Alcocer, T. Leijtens, L. M. Herz, A. Petrozza, H. J. Snaith, *Science* **2013**, *342*, 341; e) D. Liu, T. L. Kelly, *Nat Photonics* **2014**, *8*, 133; f) B. V. Lotsch, *Angew. Chem. Int. Ed.* **2014**, *53*, 635; *Angew. Chem.* **2014**, *126*, 647.
[3] T. Baikie, Y. N. Fang, J. M. Kadro, M. Schreyer, F. X. Wei, S. G. Mhaisalkar, M. Graetzel, T. J. White, *J. Mater. Chem. A* **2013**, *1*, 5628.
[4] a) Z. W. Pan, Z. R. Dai, Z. L. Wang, *Science* **2001**, *291*, 1947; b) U. Bach, D. Lupo, P. Comte, J. E. Moser, F. Weissortel, J. Salbeck, H. Spreitzer, M. Graetzel, *Nature* **1998**, *395*, 583; c) A. P. Alivisatos, *Science* **1996**, *271*, 933.
[5] E. J. W. Crossland, N. Noel, V. Sivaram, T. Leijtens, J. A. Alexander-Webber, H. J. Snaith, *Nature* **2013**, *495*, 215.
[6] G. D. Niu, W. Z. Li, F. Q. Meng, L. D. Wang, H. P. Dong, Y. Qiu, *J. Mater. Chem. A* **2014**, *2*, 705.
[7] a) A. S. Aricò, P. Bruce, B. Scrosati, J. M. Tarascon, W. Van Schalkwijk, *Nat. Mater.* **2005**, *4*, 366; b) H. Gleiter, *Acta Mater.* **2000**, *48*, 1.
[8] J. L. C. Rowsell, O. M. Yaghi, *Microporous Mesoporous Mater.* **2004**, *73*, 3.
[9] A. B. Murphy, *Sol. Energy Mater. Sol. Cells* **2007**, *91*, 1326.
[10] J. Park, K. J. An, Y. S. Hwang, J. G. Park, H. J. Noh, J. Y. Kim, J. H. Park, N. M. Hwang, T. Hyeon, *Nat. Mater.* **2004**, *3*, 891.
[11] a) F. Svec, *J. Chromatogr. A* **2010**, *1217*, 902; b) H. P. Hentze, M. Antonietti, *J. Biotechnol.* **2002**, *90*, 27.
[12] C. C. Stoumpos, C. D. Malliakas, M. G. Kanatzidis, *Inorg. Chem.* **2013**, *52*, 9019.
[13] a) K. Nakanishi, *J. Porous Mater.* **1997**, *4*, 67; b) K. Nakanishi, N. Tanaka, *Acc. Chem. Res.* **2007**, *40*, 863.
[14] a) K. Nakanishi, H. Komura, R. Takahashi, N. Soga, *Bull. Chem. Soc. Jpn.* **1994**, *67*, 1327; b) N. Tanaka, H. Kobayashi, N. Ishizuka, H. Minakuchi, K. Nakanishi, K. Hosoya, T. Ikegami, *J. Chromatogr. A* **2002**, *965*, 35.
[15] a) I. U. Arachchige, S. L. Brock, *J. Am. Chem. Soc.* **2006**, *128*, 7964; b) S. Bag, P. N. Trikalitis, P. J. Chupas, G. S. Armatas, M. G. Kanatzidis, *Science* **2007**, *317*, 490; c) N. Gaponik, A. K. Herrmann, A. Eychmüller, *J. Phys. Chem. Lett.* **2012**, *3*, 8.
[16] a) J. R. Lu, Z. X. Li, J. Smallwood, R. K. Thomas, J. Penfold, *J. Phys. Chem.* **1995**, *99*, 8233; b) M. Fujii, B. Y. Li, K. Fukada, T. Kato, T. Seimiya, *Langmuir* **2001**, *17*, 1138; c) M. A. Osman, M. Ploetze, P. Skrabal, *J. Phys. Chem. B* **2004**, *108*, 2580; d) S. Bandyopadhyay, J. C. Shelley, M. Tarek, P. B. Moore, M. L. Klein, *J. Phys. Chem. B* **1998**, *102*, 6318; e) H. Heinz, R. A. Vaia, R. Krishnamoorti, B. L. Farmer, *Chem. Mater.* **2007**, *19*, 59.
[17] D. G. Billing, A. Lemmerer, *New J. Chem.* **2008**, *32*, 1736.
[18] F. Fabregat-Santiago, J. Bisquert, L. Cevey, P. Chen, M. K. Wang, S. M. Zakeeruddin, M. Graetzel, *J. Am. Chem. Soc.* **2009**, *131*, 558.
[19] S. Polarz, *Adv. Funct. Mater.* **2011**, *21*, 3214.
[20] N. Aoyagi, Y. Furusho, T. Endo, *J. Polym. Sci. Part A* **2013**, *51*, 1230.
[21] CCDC 998856 (**1**) contains the supplementary crystallographic data for this paper. These data can be obtained free of charge from The Cambridge Crystallographic Data Centre via www.ccdc.cam.ac.uk/data_request/cif

